ATLAS Paper Draft

Search for massive supersymmetric particles in multi-jet final states produced in pp collisions at $\sqrt{s}$ = 13 TeV using the ATLAS detector at the LHC

Version: 1.0

To be submitted to: Phys. Lett. B.

Supporting internal notes

supporting note: https://cds.cern.ch/record/2242029

Comments are due by: 8 October 2017

Abstract

Results of a search for supersymmetric gluino pair production with subsequent R-parity-violating decays to quarks are presented. This search uses 36.1 fb^{-1} of data collected by the ATLAS detector in proton-proton collisions with a center-of-mass energy of $\sqrt{s}$ = 13 TeV at the LHC. The analysis is performed using requirements on the number of jets and the number of jets tagged as containing a b-hadron as well as a topological observable formed from the scalar sum of masses of large-radius jets in the event. No excess above the expected Standard Model background is observed. Limits are set on the production of gluinos in models with the R-parity-violating UDD decays of either the gluino itself (direct decay) or the neutralino produced in the R-parity-conserving gluino decay (cascade decay). In the gluino cascade decay model, gluinos with masses between 1000 GeV and 1875 GeV are excluded at 95% Confidence Level (CL), depending on the neutralino mass. For the gluino direct decay model, the 95% CL limit on the cross section times branching ratio varies between 0.80 fb^{-1} at $m_{\tilde{g}}$ = 900 GeV and 0.011 fb^{-1} at $m_{\tilde{g}}$ = 1800 GeV.

Document created on 29th September 2017 using ATLAS LaTeX Version 01-07-13.

Analysis Team

[*email:* atlas-susy-2016-22-contact-editors@cern.ch]

Brian Amadio, Samuel Bright-Thonney, Jennet Dickinson, Ian Hinchliffe, Sicong Lu, Simone Pagan-Griso, Marjorie Shapiro, Haichen Wang

Editorial Board

[*email:* atlas-susy-2016-22-editorial-board@cern.ch]

Christopher John Young (chair), Teresa Barillari, Francesco De Lorenzi, Andre Sopczak

ATLAS PAPER

ATLAS-SUSY-2016-022

29th September 2017

Draft version 1.0

Search for massive supersymmetric particles in multi-jet final states produced in pp collisions at $\sqrt{s}$ = 13 TeV using the ATLAS detector at the LHC

The ATLAS Collaboration

Abstract

Results of a search for supersymmetric gluino pair production with subsequent R-parity-violating decays to quarks are presented. This search uses 36.1 fb^{-1} of data collected by the ATLAS detector in proton-proton collisions with a center-of-mass energy of $\sqrt{s}$ = 13 TeV at the LHC. The analysis is performed using requirements on the number of jets and the number of jets tagged as containing a b-hadron as well as a topological observable formed from the scalar sum of masses of large-radius jets in the event. No excess above the expected Standard Model background is observed. Limits are set on the production of gluinos in models with the R-parity-violating UDD decays of either the gluino itself (direct decay) or the neutralino produced in the R-parity-conserving gluino decay (cascade decay). In the gluino cascade decay model, gluinos with masses between 1000 GeV and 1875 GeV are excluded at 95% Confidence Level (CL), depending on the neutralino mass. For the gluino direct decay model, the 95% CL limit on the cross section times branching ratio varies between 0.80 fb^{-1} at $m_{\tilde{g}}$ = 900 GeV and 0.011 fb^{-1} at $m_{\tilde{g}}$ = 1800 GeV.

To be submitted to: *Phys. Lett. B.*

1 Introduction

Supersymmetry (SUSY) [1–6] is a theoretical extension of the Standard Model (SM) which fundamentally relates fermions and bosons. It is an alluring theoretical possibility given its potential to solve the naturalness problem [7, 8].

This note presents a search for R-parity-violating (RPV) [9–14] supersymmetric gluino pair production with subsequent decays to quarks in events with many jets using 36.1 fb^{-1} of pp collision data at $\sqrt{s}$ = 13 TeV collected by the ATLAS detector in 2015 and 2016. In supersymmetry, the RPV component of a generic super pontential can be written as [15, 16]:

$$W_{\not R_p} = \tfrac{1}{2}\lambda_{ijk} L_i L_j \bar{E}_k + \lambda'_{ijk} L_i Q_j \bar{D}_k + \tfrac{1}{2}\lambda''_{ijk} \bar{U}_i \bar{D}_j \bar{D}_k + \kappa_i L_i H_2, \quad (1)$$

where $i, j, k = 1, 2, 3$ are generation indices. The generation indices are sometimes omitted in the discussions that follow if the statement being made is not specific to any generation. The first three terms in Eq. (1) are often referred to as the trilinear couplings, whereas the last term is referred to as bilinear. The L_i, Q_i represent the lepton and quark $SU(2)_{\mathrm{L}}$ doublet superfields, whereas H_2 represents the Higgs superfield. The $\bar{E}_j$, $\bar{D}_j$, and $\bar{U}_j$ are the charged lepton, down-type quark, and up-type quark $SU(2)_{\mathrm{L}}$ singlet superfields, respectively. The couplings for each term are given by λ, λ', and λ'', and κ is a dimensional mass parameter. In the benchmark models considered in this search, only the baryon-number-violating coupling λ''_{ijk} is non-zero, in order to protect the proton from rapid decay. Because of the structure of Eq. (1), scenarios in which only $\lambda''_{ijk} \neq 0$ are often referred to as UDD scenarios. The diagrams shown in Figure 1 represent the benchmark processes used in the optimization and design of the search presented in this note. In the gluino direct decay model (Figure 1(a)), the gluino directly decays to three quarks via the RPV UDD coupling λ'', leading to six quarks at the tree-level in the final state of gluino pair production. In the gluino cascade decay model (Figure 1(b)), the gluino decays to two quarks and a neutralino, which, in turn, decays to three quarks via the RPV UDD coupling λ'', resulting in ten quarks at the tree-level in the final state of gluino pair production. Events produced in these processes typically have a high multiplicity of reconstructed jets.In signal models considered in this search, the production of the gluino pair is assumed to be independent of the value of λ''. All possible λ'' flavor combinations given by the structure of Eq. (1) are assumed to proceed with equal probability, and decays of the gluino and neutralino are assumed to be prompt.[1] Under this configuration, a significant portion of signal events contain at least one bottom or top quark. Other models of the RPV UDD scenario, such as the Minimum Flavor Violation model [17, 18], also predict that the gluino decays preferably to final states with third generation quarks. These theoretical arguments motivate the introduction of b-tagging requirements to the search.

This analysis is an update to previous ATLAS searches for signals arising from RPV UDD scenarios [19, 20] performed with data taken during LHC Run-1. The search strategy follows closely the one implemented in Ref. [20], which has excluded a gluino with mass up to 917 GeV in the gluino direct decay model, and a gluino with mass up to 1 TeV for a neutralino mass of 500 GeV in the gluino cascade decay model.

In a recent publication [21], the CMS collaboration also sets a limit on the gluino mass up to 1.03 TeV in a RPV UDD scenario where the gluino exclusively decays to a final state of a top quark, a bottom quark and a strange quark, using $\sqrt{s}$ = 8 TeV pp collision data.

[1] While the signal models used for interpretation assume prompt decays of supersymmetric particles, the analysis selection does not explicitly reject non-prompt jets.

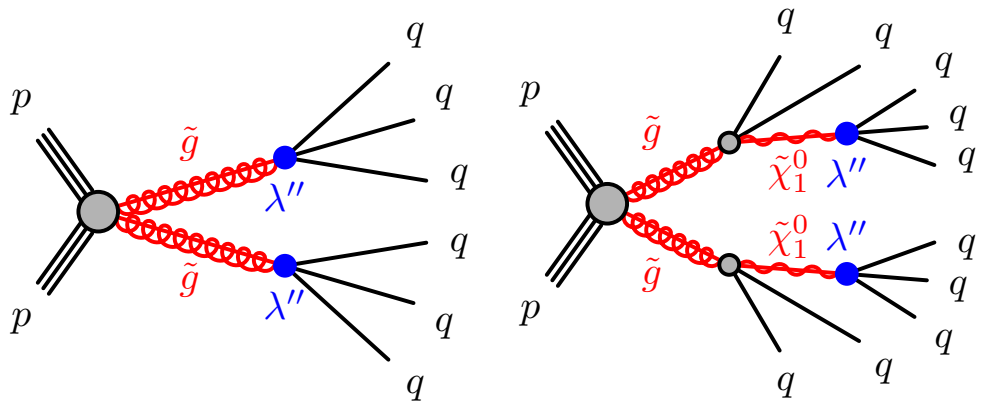

(a) gluino direct decay model (b) gluino cascade decay

Figure 1: Diagrams for the benchmark processes considered for this analysis. The black lines represent Standard Model particles, the red lines represent SUSY partners, the gray shaded circles represent effective vertices that include off-shell propagators (e.g. heavy squarks coupling to a $\tilde{\chi}_1^0$ neutralino and a quark), and the blue solid circles represent effective RPV vertices allowed by the baryon-number-violating λ'' couplings with off-shell propagators (e.g. heavy squarks coupling to two quarks). Quark and anti-quark are not distinguished in the diagrams.

2 ATLAS detector

The ATLAS detector [22] covers almost the whole solid angle around the collision point with layers of tracking detectors, calorimeters and muon chambers. For the measurements presented in this note, the calorimeters are of particular importance. The inner detector, immersed in a magnetic field provided by a solenoid, has full coverage in ϕ and covers the pseudorapidity range $|\eta| < 2.5$.[2] It consists of a silicon pixel detector, a silicon microstrip detector and a transition radiation straw-tube tracker. The innermost pixel layer [23] was added between Run-1 and Run-2 of the LHC, around a new thinner (radius of 25 mm) beam pipe. In the pseudorapidity region $|\eta| < 3.2$, high granularity lead liquid-argon (LAr) electromagnetic (EM) sampling calorimeters are used. A steel-scintillator tile calorimeter provides hadronic calorimetry coverage over $|\eta| < 1.7$. The end-cap and forward regions, spanning $1.5 < |\eta| < 4.9$, are instrumented with LAr calorimetry for both EM and hadronic measurements. The muon spectrometer surrounds these calorimeters, and comprises a system of precision tracking chambers and trigger detectors with three large toroids, each consisting of eight coils providing the magnetic field for the muon detectors. A two-level trigger system is used to select events [24]. The first-level trigger is implemented in hardware and uses a subset of the detector information. This is followed by the software-based High-Level Trigger, which can run offline reconstruction and calibration software, reducing the event rate to about 1 kHz.

[2] ATLAS uses a right-handed coordinate system with its origin at the nominal interaction point in the center of the detector and the z-axis along the beam direction. The x-axis points toward the center of the LHC ring, and the y-axis points upward. Cylindrical coordinates (r, ϕ) are used in the transverse plane, ϕ being the azimuthal angle around the beam pipe. The pseudorapidity η is defined in terms of the polar angle θ by $\eta \equiv -\ln[\tan(\theta/2)]$.

3 Simulation samples

Signal samples are produced covering a wide range of gluino and neutralino masses. In the gluino direct decay model, the gluino mass ($m_{\tilde{g}}$) is varied from 900 GeV to 1800 GeV. In the case of the cascade decays, for each gluino mass (1000 GeV to 2100 GeV), separate samples are generated with multiple neutralino masses ($m_{\tilde{\chi}_1^0}$) ranging from 50 GeV to 1.65 TeV. In each case, $m_{\tilde{\chi}_1^0} < m_{\tilde{g}}$. In the gluino cascade decay model, the two quarks produced from the gluino decay are restricted to be the first or second generation quarks. All three generations of quarks are allowed to be in the final state of the lightest supersymmetric particle decay. Signal samples are generated at the leading order (LO) accuracy with up to two additional partons using the MadGraph5_aMC@NLO v2.3.3 event generator [25] interfaced to Pythia 8.186 [26]. The A14 [27] tune is used together with the NNPDF2.3LO [28] parton distribution function (PDF) set. The EvtGen v1.2.0 program [29] is used to describe the properties of the b- and c- hadron decays in the signal samples The signal production cross sections are calculated at next-to-leading order (NLO) in the strong coupling constant, adding the resummation of soft gluon emission at next-to-leading-logarithmic accuracy (NLO+NLL) [30–34]. The nominal cross section and its uncertainty are taken from Ref. [35]. cross sections are evaluated assuming masses of 450 TeV for the light-flavour squarks in case of gluino pair production. In the simulation, the total widths of gluino and neutralino are set to be 1 GeV, effectively making their decays prompt.

While a data-driven method is used to estimate the background, simulated events are used to establish, test and validate the methodology of the analysis. Therefore, simulation is not required to precisely describe the background, but it should be sufficiently similar that the strategy can be tested before applying it to data. Multi-jet events constitute the dominant background in the search region, with small contributions from top-quark pair-production ($t\bar{t}$). Contributions from γ + jets, W + jets, Z + jets, single-top quark, and diboson background processes are found to be negligible from simulation studies.

The multijet background is studied with three different Monte Carlo samples. The Pythia 8.186 generator is used together with the A14 tune and the NNPDF2.3LO parton distribution functions, while the Herwig++ 2.7.1 generator is used together with the UEEE5 tune and CTEQ6L1 [36] PDF sets. Sherpa multi-jet samples are also generated and tested for the background estimation. Matrix elements are calculated with up to 3 partons at LO and merged with the Sherpa parton shower [37] using the ME+PS@LO prescription [38]. The EvtGen v1.2.0 program [29] is also used to describe the properties of the b- and c- hadron decays for the background samples except those generated with Sherpa [39]. The CT10 PDF set [40] is used in conjunction with dedicated parton shower tuning developed by the Sherpa authors.

For the generation of fully hadronic decaying $t\bar{t}$ events, the Powheg-Box v2 [41] generator is used with the CT10 PDF set. The parton shower, fragmentation, and the underlying event are simulated using Pythia 6.428 [42] with the CTEQ6L1 PDF set [36] and the corresponding Perugia 2012 tune (P2012) [43].

The effect of additional pp interactions per bunch crossing ("pile-up") as a function of the instantaneous luminosity is taken into account by overlaying simulated minimum-bias events according to the observed distribution of the number of pile-up interactions in data. All Monte-Carlo (MC) simulated background samples are passed through a full GEANT4 [44] simulation of the ATLAS detector [45]. The signal samples are passed through a fast detector simulation based on a parameterization of the performance of the ATLAS electromagnetic and hadronic calorimeters [46] and on GEANT4 elsewhere. The consistency between the fast simulation sample and full simulation sample is validated at a number of signal points in the $m_{\tilde{g}}$-$m_{\tilde{\chi}_1^0}$ plane considered in this paper.

4 Event selection

The data were recorded in 2015 and 2016, with the LHC operating at a center-of-mass energy of $\sqrt{s}$ = 13 TeV. All detector elements are required to be fully operational. The integrated luminosity is measured to be 3.2 fb^{-1} and 32.9 fb^{-1}, for the 2015 and 2016 data sets, respectively. The uncertainty in the combined 2015 and 2016 integrated luminosity is 2.1%. It is derived, following a methodology similar to that detailed in Ref. [47], from a preliminary calibration of the luminosity scale using x-y beam-separation scans performed in August 2015 and May 2016.

The events used in this search are selected using a H_{T} trigger, which requires the scalar sum of jet p_{T} to be greater than 1.0 TeV. This requirement is found to be fully efficient for signal samples considered in this paper. Events are required to have a primary vertex with at least two associated tracks with p_{T} above 0.4 GeV. The primary vertex assigned to the hard-scattering collision is the one with the highest $\sum_{\mathrm{track}} p_{\mathrm{T}}^2$, where the scalar sum of track p_{T}^2 is taken over all tracks associated with that vertex.

Jets are reconstructed from three-dimensional topological clusters of energy deposits in the calorimeter calibrated at the EM scale [48], using the anti-kt algorithm with two different radius parameters of $R = 1.0$ and $R = 0.4$, hereafter referred to as large-R jets and small-R jets, respectively. The four-momenta of the jets are calculated as the sum of the four-momenta of the clusters, which are assumed to be massless. For the large-R jets, the original constituents are calibrated using the local cluster weighting algorithm [49] prior to jet finding and reclustered using the longitudinally-invariant k_t algorithm [50] with a radius parameter of $R_{sub-jet} = 0.2$, to form a collection of sub-jets. A sub-jet is discarded if it carries less than 5% of the p_{T} of the original jet. The constituents in the remaining sub-jets are then used to recalculate the large-R jet four-momenta, and the jet energy and mass are further calibrated to particle level using correction factors derived from simulation [51]. The resulting "trimmed" [51, 52] large-R jets are required to have $p_{\mathrm{T}} > 200$ GeV and $|\eta| < 2.0$. The analysis selects events with at least three large-R jets and requires the p_{T} of the leading large-R jet to be greater than 440 GeV so that the trigger is fully efficient with respect to the analysis selection. Events with three large-R jets are used to derive jet mass templates. Events with higher large-R jet multiplicity are used to validate background estimation performance and probe the existence of Beyond SM (BSM) signals. The small-R jets are corrected for pile-up contributions and are then calibrated to the particle level using simulation followed by a correction based on in-situ measurements [53, 54].

The identification of jets containing b-hadrons is based on the small-R jet with $p_{\mathrm{T}} > 50$ GeV and $|\eta| < 2.5$ and a multivariate tagging algorithm [55, 56]. This algorithm is applied to a set of tracks with loose impact parameter constraints in a region of interest around each jet axis to enable the reconstruction of the b-hadron decay vertex. The b-tagging requirements result in an efficiency of 70% for jets containing b-hadrons, as determined in a sample of simulated $t\bar{t}$ events [56]. A small-R jet passing the b-tagging requirement is considered as a b-jet.

The analysis of data is primarily based on observables built from large-R jets, and the small-R jets are only used to classify events or large-R jets based on the b-tagging information. Specifically, events selected in the analysis are divided to a `b-tag` sample where at least one b-jet is present in the event, and a `b-veto` sample where no b-jet is present in the event. Events selected without a b-tagging requirement are referred to as `inclusive` events. Large-R jets are classified to those that can be matched to a b-jet within $\Delta R = 1.0$ (b-matched jets), and those that cannot be matched to a b-jet.

5 Analysis strategy

The analysis uses a topological observable, the total jet mass variable, M_{J}^{Σ}, as the primary discriminating variable to separate signal and background. The observable M_{J}^{Σ} [57–59] is defined as the scalar sum of the masses of the four leading large-R jets reconstructed with a radius parameter $R = 1.0$, $p_{\mathrm{T}} > 200$ GeV and $|\eta| < 2.0$,

$$M_{\mathrm{J}}^{\Sigma} = \sum_{\substack{p_{\mathrm{T}}>200\,\mathrm{GeV} \\ |\eta|\leq 2.0}}^{4} m^{\mathrm{jet}}. \tag{2}$$

This observable was used for the first time in the $\sqrt{s} = 8$ TeV search by the ATLAS Collaboration for events with many jets and missing transverse momentum [60] and provides significant sensitivity for very high-mass gluinos. It was also used in the search by the ATLAS Collaboration for RPV SUSY in events with many jets using the Run-1 LHC data [20]. Here, the four leading jets in the event are used, as they cover a significant portion of the central region of the calorimeter, and are very likely to capture most signal quarks.

Simulation studies show that M_{J}^{Σ} provides greater sensitivity than variables such as H_{T} or the scalar sum of jet p_{T}. The masses contain angular information about the events, whereas a variable like H_{T} simply describes the energy (or transverse momentum) in the event. A large M_{J}^{Σ} implies not only high energy of the mult-jet system, but also rich angular structure [57, 58]. Figure 2(a) presents examples of the discrimination that the M_{J}^{Σ} observable provides between the background (represented here by Sherpa and Pythia 8.186 multi-jet MC simulation) and several signal samples, as well as the comparison of the data to the Monte Carlo multi-jet background.

Another discriminating variable that is independent of M_{J}^{Σ} is necessary in order to define suitable control and validation regions where the background estimation can be studied and tested. The signal is characterized by a higher rate of central jet events as compared to the primary multi-jet background. This is expected due to the difference in the production processes that is predominantly s-channel for the signal, while the background can also be produced through u- and t-channel processes. Figure 2(b) shows the distribution of the pseudorapidity difference between the two leading large-R jets, $|\Delta\eta_{12}|$ for several signal and background Monte Carlo samples, as well as data. A high $|\Delta\eta_{12}|$ requirement can be applied to establish a control region or a validation region where the potential signal contamination needs to be suppressed.

The use of M_{J}^{Σ} in this analysis provides an opportunity to employ the fully data-driven jet mass *template method* to estimate the background contribution in signal regions. The jet mass template method is discussed in Ref. [59], and its first experimental implementation is described in Ref. [20]. In this method, single jet mass templates are extracted from signal-depleted control regions. These jet mass templates are created in bins that are defined by a number of observables, which include jet p_{T} and $|\eta|$, and the b-matching status. They provide a *probability density function* that describes the relative probability for a jet with a given p_{T} and η to have a certain mass. This method assumes that jet mass templates only depend on these observables and are the same between control regions and signal regions. A sample where the background M_{J}^{Σ} distribution needs to be estimated, such as a validation region or a signal region, is referred to as the kinematic sample. The only information used is the jet p_{T} and η, as well as its b-matching status, which are inputs to the templates. For each jet in the kinematic sample, its

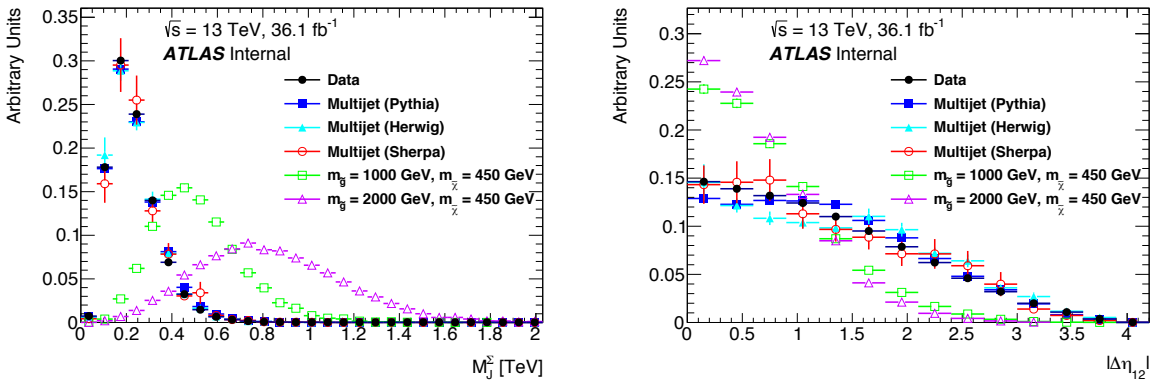

(a) M_{J}^{Σ} (b) $|\Delta\eta_{12}|$

Figure 2: Comparison between signal sample and background dominant data control sample for (a) the scalar sum of the masses of the four leading large-R jets M_{J}^{Σ} and (b) the difference in pseudorapidity between the two leading large-R jets $|\Delta\eta_{12}|$. Several typical signal points are shown, as well as the distributions obtained from the data. All distributions are normalized to the same area. The selection requires four or more jets, is inclusive in $|\Delta\eta_{12}|$ and has no b-tagging requirements.

corresponding jet mass template is sampled to generate a random jet mass. A M_{J}^{Σ} distribution can be constructed from the randomized jet masses of the kinematic sample. If jet mass templates are created from a control sample of background events and the number of events in the kinematic sample is sufficiently large, then the M_{J}^{Σ} distribution constructed from randomized jet masses should reproduce the shape of the M_{J}^{Σ} distribution for the background.

This jet mass prediction procedure is similar to the one employed in Ref. [20] with two minor differences. First, the statistical fluctuations in the jet mass templates is propagated to the prediction of background yield in the signal region, and therefore considered as a systematic uncertainty of the jet mass template method, whereas the Run-1 analysis smoothed the jet mass templates with a Gaussian kernel technique. Second, the predicted M_{J}^{Σ} distribution is normalized to the observation in 0.2 TeV < M_{J}^{Σ} < 0.6 TeV, whereas the Run-1 analysis did not introduce any normalization region, effectively normalizing the prediction to the observation in the entire M_{J}^{Σ} range. In the region of 0.2 TeV < M_{J}^{Σ} < 0.6 TeV, contamination from signal models not yet excluded by the ATLAS Run-1 search [20] is negligible compared to the statistical uncertainty of background.

The selected events are divided into control, uncertainty determination validation and signal regions, as summarized in Table 1. Control regions (CRs) are defined with events that have three large-R jets with p_{T} > 200 GeV. Jets in the control region are divided into 4 $|\eta|$ bins uniformly defined between 0 and 2, 15 p_{T} bins uniformly defined in $\log(p_{\mathrm{T}})$, and two b-matching status bins (b-matched or not). A total of 120 jet mass templates are created. Figure 3 shows example jet mass template distribtuions in two p_{T}-$|\eta|$ bins for both data and Pythia multijet samples. The shape of jet mass template is evidently different between b-matched jets and non-matched jets. A $|\Delta\eta_{12}|$ > 1.4 requirement is included for the control region of b-matched jets to suppress potential signal contamination. For each control region, a variable binning in jet p_{T} and η is chosen to ensure that every jet mass template has a sufficiently large number of jets.

Four overlapping signal regions (SRs) are considered in this analysis. All signal regions are required to have $|\Delta\eta_{12}|$ < 1.4. The first set of signal regions does not require the presence of a b-jet and is used to test

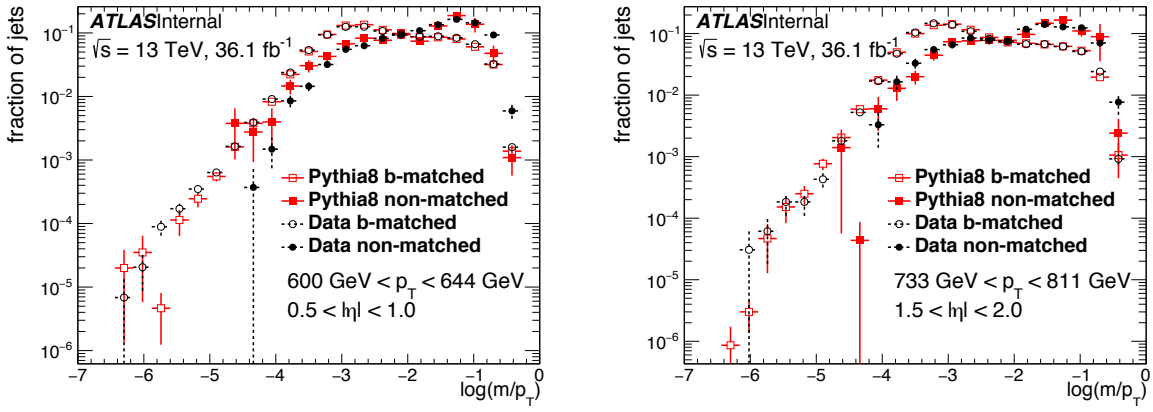

(a) 600 GeV < p_{T} < 644 GeV, 0.5 < $|\eta|$ < 1.0

(b) 733 GeV < p_{T} < 811 GeV, 1.5 < $|\eta|$ < 2.0

Figure 3: Example jet mass template distributions for b-matched jets (black dots) and non-matched jets (red squares) in data and PYTHIA multijet samples. (a) shows the jet mass template distributions in the bin of 600 GeV < p_{T} < 644 GeV, 0.5 < $|\eta|$ < 1.0, while (b) shows the jet mass template distributions in the bin of 733 GeV < p_{T} < 811 GeV, 1.5 < $|\eta|$ < 2.0.

more generic BSM signals of pair-produced heavy particles cascade decaying to many quarks or gluons. Two selections on the large-R jet multiplicity are used, $N_{\mathrm{jet}} \geq 4$ (4jSR) and $N_{\mathrm{jet}} \geq 5$ (5jSR). In order to further improve the sensitivity to the benchmark signal models of RPV UDD scenario, subsets of events in the 4jSR and 5jSR are selected by requiring the presence of at least one b-tagged small-R jet. To ensure the H_{T} trigger is fully efficient for the offline data analysis, a leading jet $p_{\mathrm{T}} > 400$ GeV requirement is added for signal regions with four or more large-R jets. Finally, a cut on the M_{J}^{Σ} variable is placed in each signal region, with the cut value optimized for the direct and cascade decay models considered in this paper. For each signal region a validation region is defined by reversing the $|\Delta\eta_{12}|$ requirement. These validation regions are used to cross check the background estimation, thus validating the background prediction in the signal region.

Uncertainties of the jet mass prediction includes a statistical component and a systematic component. The statistical uncertainty arises from the limited sample size in the control region, and the statistical nature of the jet mass randomization, which can be quantified through pseudo-experiment. Systematic uncertainties of the jet mass prediction can be attributed to a number of factors, for example, jet mass templates are assumed to only depend on a finite number of observables (jet p_{T} $|\eta|$, and b-matching information, in this analysis), jet mass templates are created for each of these observables with a finite bin width, and jets in the same event are assumed to be uncorrelated and their masses can be modeled independently, etc.. These systematic uncertainties are estimated in uncertainty determination regions (UDRs) in data, where the predicted and observed jet masses are compared. The difference between them provides an estimate of the size of the systematic uncertainty.

One UDR (UDR1) is defined by requiring exactly two large-R jets with the p_{T} of leading large-R jet greater than 400 GeV. Events in this UDR contains high p_{T} jets and can have an imbalance in p_{T} between the leading jet and the subleading jet. The other UDR (UDR2) is defined by requiring exactly four large-R jets with the p_{T} of leading large-R jet less than 400 GeV. Events in this UDR contain less energetic and tend to be more balanced in p_{T}. In each UDR, selected jets are binned in the same way as they are in the control regions.

		N_{jet} (p_{T} > 200 GeV)	b-tag	$p_{T,1}$	$\lvert\Delta\eta_{12}\rvert$	M_{J}^{Σ}
CR	3jCR	= 3	-	-	-	-
UDR	UDR1	= 2	-	> 400 GeV	-	-
	UDR2	= 4	-	< 400 GeV	-	-
VR	4jVRb	≥ 4	Yes	> 400 GeV	> 1.4	-
	5jVRb	≥ 5	Yes	-	> 1.4	-
	4jVR	≥ 4	-	> 400 GeV	> 1.4	-
	5jVR	≥ 5	-	-	> 1.4	-
SR	4jSRb	≥ 4	Yes	> 400 GeV	< 1.4	> 1.0 TeV
	5jSRb	≥ 5	Yes	-	< 1.4	> 0.8 TeV
		≥ 5	Yes	-	< 1.4	> 0.6 TeV
	4jSR	≥ 4	-	> 400 GeV	< 1.4	> 1.0 TeV
	5jSR	≥ 5	-	-	< 1.4	> 0.8 TeV

Table 1: Summary of the event level and jet level requirements used to define various regions. Requirements on large-R jet multiplicity (N_{jet}), whether or not a b-jet is present (b-tag), and the pseudo-rapidity gap between the two leading jets ($|\Delta\eta_{12}|$) are applied to define control, validation and signal regions. In addition, each signal region includes an additional M_{J}^{Σ} cut for statistical interpretation, and control regions are defined separately for non-matched jets and b-matched jets. For the uncertainty determination regions, the N_{jet} and leading jet p_{T} ($p_{T,1}$) requriements are used.

In order to quantify the small discrepancy between the predicted jet mass and the observed one, the jet mass response, defined as the ratio of the average of observed jet mass over the average of predicted jet mass, is studied with both UDRs. It is found that the discrepancy of jet mass distributions in the same p_{T} and $|\eta|$ bin between different regions can be largely captured by a shift between the distributions, and therefore the jet mass response reflects the size of this shift. Studies using Monte Carlo multijet events have shown that scaling up and down the predicted jet mass by the jet mass response in the UDRs leads to variations in the predicted M_{J}^{Σ} distribution that can cover the difference between the observed and predicted M_{J}^{Σ} distributions.

Figure 4 shows the jet mass responses in the UDRs as a function of jet p_{T} and $|\eta|$. An under-prediction of jet mass is seen in the UDR1, varying between a few percent and 14%. In the p_{T} range of 200 GeV - 400 GeV, the UDR2 indicates an over-prediction, at 4 - 5% level. Overall, the behavior of jet mass response is quite similar between different pseudo-rapidity regions. The discrepancies in the jet mass response are used as an estimate for the p_{T}- and $|\eta|$- dependent systematic uncertainty of the jet mass prediction. Since the signs of the discrepancies of the UDR1 and UDR2 are opposite in the p_{T} range of 200 GeV - 400 GeV, the larger discrepancy between these UDRs are used as the uncertainty. The uncertainty of jet mass prediction is uncorrelated between the p_{T} range of 200 GeV - 400 GeV ("low p_{T}") and the p_{T} range of > 400 GeV ("high p_{T}"). For jets in the same p_{T} ranges, the jet mass prediction uncertainty is correlated between different p_{T} and $|\eta|$ bins.

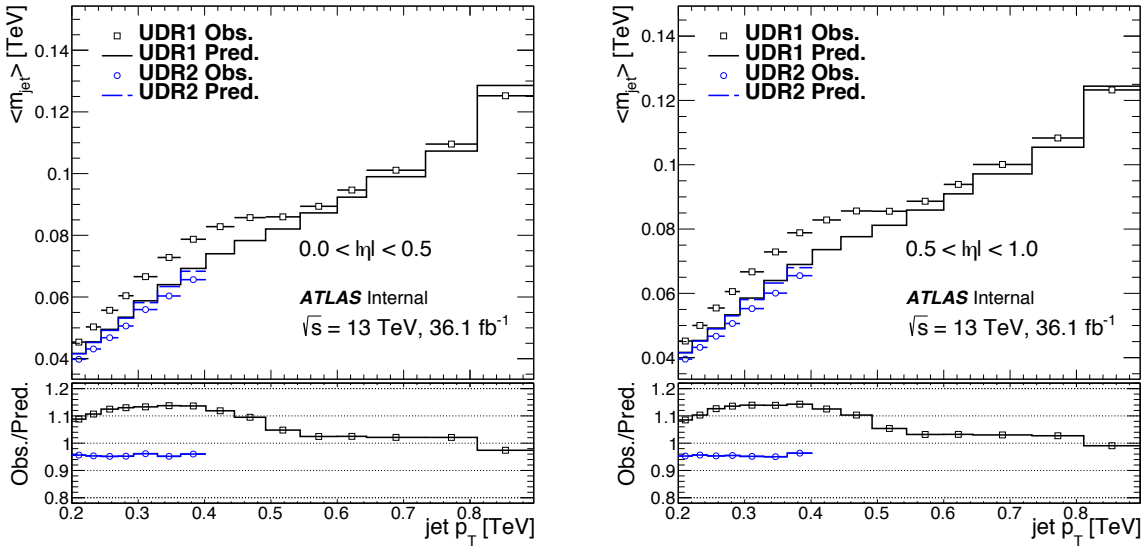

(a) $|\eta| < 0.5$

(b) $0.5 < |\eta| < 1.0$

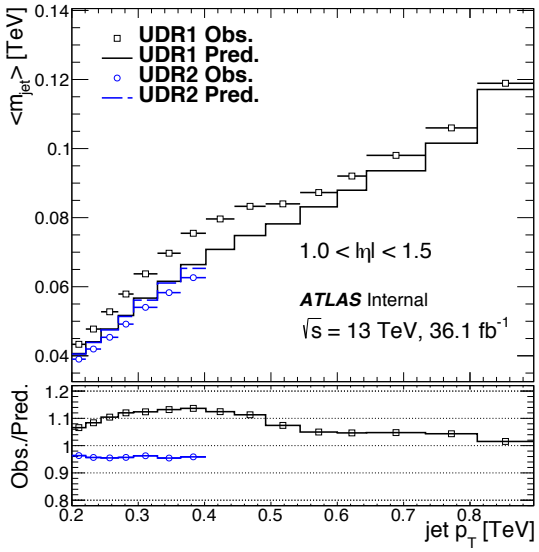

(c) $1.0 < |\eta| < 1.5$

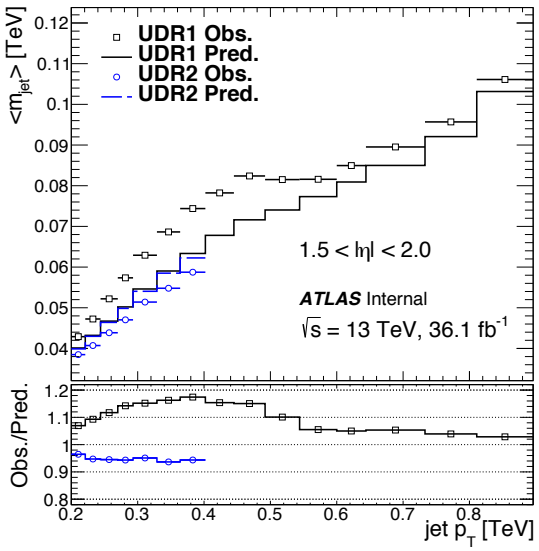

(d) $1.5 < |\eta| < 2.0$

Figure 4: The average observed and predicted jet masses (top panes) and the jet mass responses (bottom pane) in the UDR1 and UDR2 are shown for four different pseudorapidity regions.

Possible effects induced in the background estimation by the presence of massive objects from top pair production are not explicitly addressed by the background estimation strategy. However, a study using Monte Carlo multijet and $t\bar{t}$ samples finds that the background prediction is insensitive to the presence of $t\bar{t}$ events, because of its relatively small cross section.

The jet mass template method is then applied to data in the validation and signal regions. Uncertainties on the jet mass prediction derived from the UDRs are propagated to the predicted M_J^{Σ} distribution. The background estimation performance is first examined in the validation regions. Figure 5 shows the

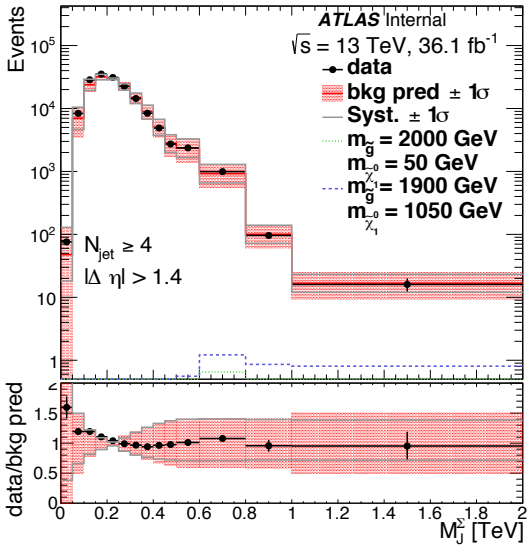

(a) ≥ 4 jets, `inclusive` events (4jVR)

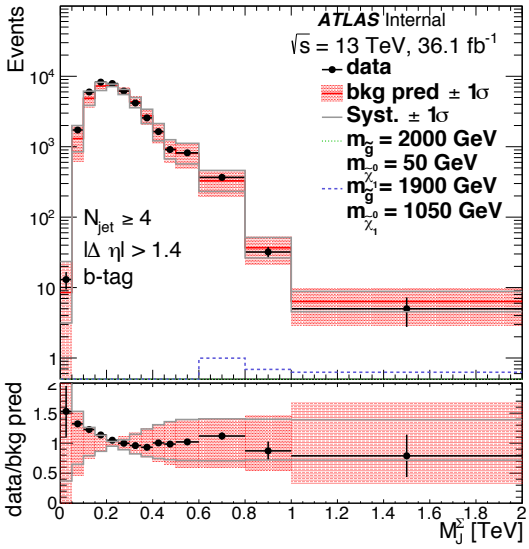

(b) ≥ 4 jets, `b-tag` events (4jVRb)

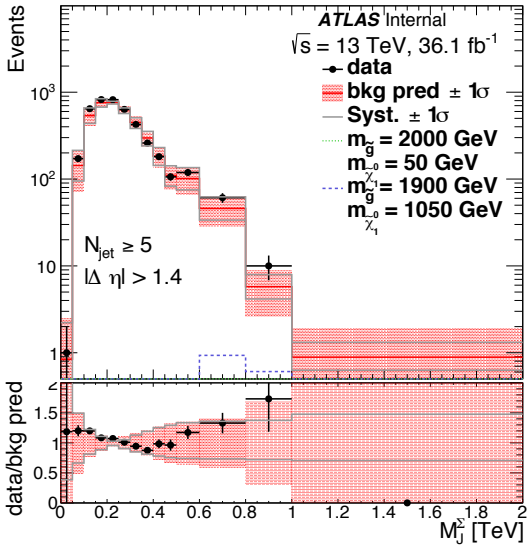

(c) ≥ 5 jets, `inclusive` events (5jVR)

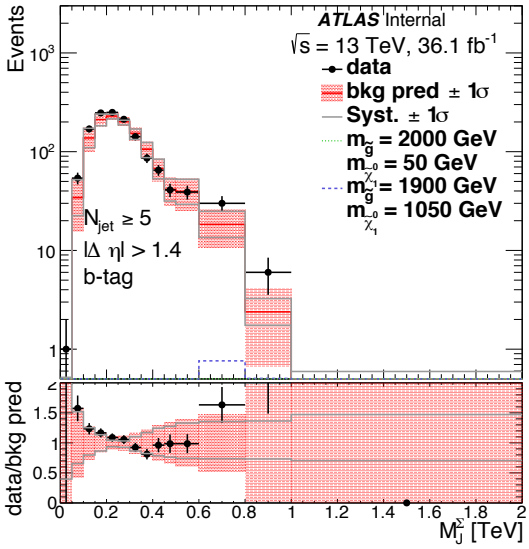

(d) ≥ 5 jets, `b-tag` events (5jVRb)

Figure 5: Predicted (solid line) and observed (dots) M_J^Σ distributions for validation regions 4jVR (a), 4jVRb (b), 5jVR (c), and 5jVRb (d). The shaded area surrounding the predicted M_J^Σ distribution represents the uncertainty of the background estimation. The dressed M_J^Σ distribution is normalized to data in 0.2 TeV < M_J^Σ < 0.6 TeV, where expected contamination from signals of gluino direct or cascade decay models not excluded by the Run-1 analysis [20] is negligible compared to the background statistical uncertainty. The expected contribution from two RPV signal samples are also shown.

observed and predicted M_J^Σ distributions in the validation regions, where in general a good agreement between them is seen. The difference between the observed and predicted M_J^Σ distribution is consistent with variations of jet mass prediction due to correlated systematic uncertainties and is covered by the total uncertainty. Figure 6 shows the dressed and predicted M_J^Σ distributions in signal regions.

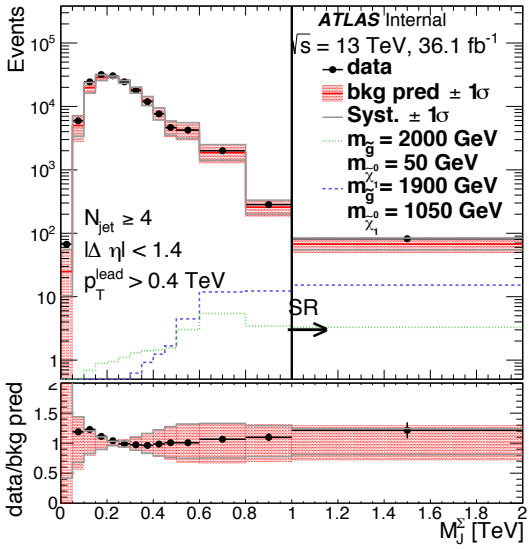

(a) ≥ 4 jets, `inclusive` events (4jSR)

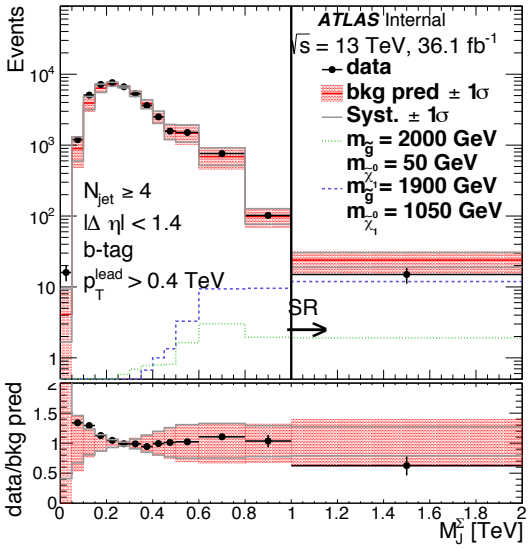

(b) ≥ 4 jets, `b-tag` events (4jSRb)

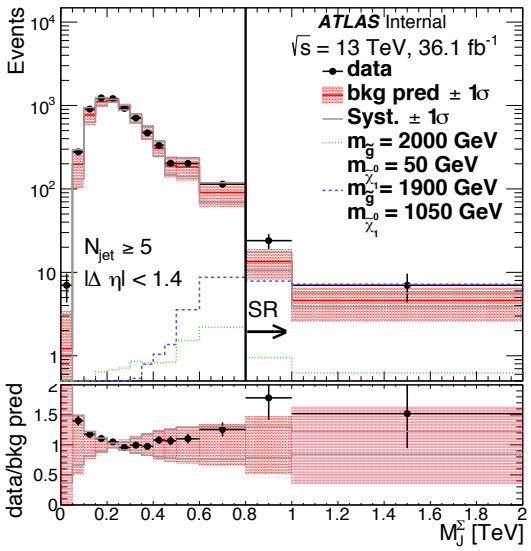

(c) ≥ 5 jets, `inclusive` events (5jSR)

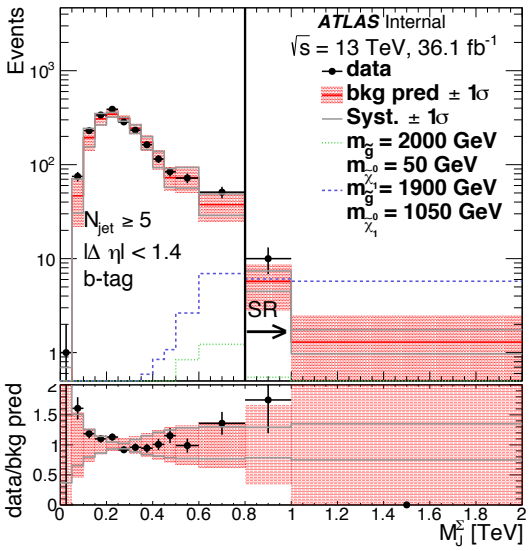

(d) ≥ 5 jets, `b-tag` events (5jSRb)

Figure 6: Predicted (solid line) and observed (dots) M_J^Σ distributions for signal regions 4jSR (a), 4jSRb (b), 5jSR (c), and 5jSRb (d). The shaded area surrounding the predicted M_J^Σ distribution represents the uncertainty of background estimation. The predicted M_J^Σ distribution is normalized to data in 0.2 TeV < M_J^Σ < 0.6 TeV, where expected contamination from signals of gluino direct or cascade decay models not excluded by the Run-1 analysis [20] is negligible compared to the background statistical uncertainty. The expected contribution from two RPV signal samples are also shown.

The statistical interpretation is based on the event yield in a signal region beyond an M_J^Σ threshold, which should maximize the sensitivity to the both gluino direct and cascade decay models. For the 5jSR and 5jSRb, the threshold used is 0.8 TeV, except that for direct decay models with $m_{\tilde{g}} < 1080$ GeV, 5jSRb with $M_J^\Sigma > 0.6$ TeV is found to be the most optimal. For the 4jSR and 4jSRb, the M_J^Σ threshold is 1.0 TeV. The

model-dependent interpretation is performed in all the signal regions with the M_J^Σ cuts mentioned just above.

6 Signal systematic uncertainties

The main systematic uncertainties for the predicted signal yield include the large-R jet mass scale and resolution uncertainties, b-tagging uncertainty, Monte Carlo statistical uncertainty, and luminosity uncertainty. The large-R jet mass scale and resolution uncertainty is as large as 24% for signal models with $m_{\tilde{g}}$ = 1000 GeV, and drops to $\approx$ 8% for signal models with $m_{\tilde{g}}$ =1800 GeV. The Monte Carlo samples reproduce the b-tagging efficiency measured in data with limited accuracy. Dedicated correction factors, derived from a comparison between data and MC in $t\bar{t}$ events, are applied to the signal samples. The uncertainty of the correction factors is propagated to a systematic uncertainty on the yields in the signal region. This uncertainty is between 1% and 5% for all signal models considered in this analysis. Due to low acceptance, the statistical uncertainty of the signal yield predicted by the Monte Carlo samples can be as large as 8% for signal models with $m_{\tilde{g}} \leq 1000$ GeV. The Monte Carlo statistical uncertainty for signal models with large $m_{\tilde{g}}$ is negligible. Uncertainties on the signal acceptance due to the choices of PDF, QCD scales and the modeling of initial state radiation (ISR) are studied. The uncertainty of PDF and QCD scales is found to be up to 25% for $m_{\tilde{g}} \approx 1000$ GeV, and a few percent for $m_{\tilde{g}} \approx 2100$ GeV.

Since signal events have different kinematic distributions and jet flavor composition than the background events, the presence of signal events in data can bias the predicted background yield in the signal region. The contribution to the predicted background yield due to the presence of signal events can be known by studying signal Monte Carlo samples, and therefore is subtracted from the background prediction for the model-dependent interpretation. This pontential bias is not considered for the model-independent interpretation. As the contribution is induced by the signal events, the correction also scales with the size of the signal events, which is equivalent to a correction on the predicted signal yield. The size of the correction relative to the predicted signal can be as large as $\approx$ 50% for cascade decay models with $m_{\tilde{g}}$ =2000 GeV, $m_{\tilde{\chi}_1^0}$ =50 GeV, and goes down to a few percents for models with small mass splitting between the gluino and neutralino.

7 Results

Table 2 summarizes the predicted and observed event yields in signal regions with different M_J^Σ cuts, which are used to construct the likelihood function for the statistical interpretation. Modest excesses are seen in signal regions requiring five or more jets and the signal region of 4jSR.

Signal and background systematic uncertainties are incorporated as nuisance parameters. A frequentist procedure based on the profile likelihood ratio [61] is used to evaluate the p_0-values of these excesses, and the results are shown in Table 3. Since no significant excess is seen in any of the signal regions, a model-independent limit on σ_{vis}, defined as the cross section times acceptance times efficiency of a generic BSM model, is calculated using the modified frequentist CL_s method [62]. The observed and expected limits are shown in Table 3.

Limits are also set on the production of RPV signals in the context of gluino direct and cascade decay models and are shown in Figure 7. Typically, for RPV signals from the gluino cascade decay model with

Region	$\geq M_J^\Sigma$ [TeV]	Observed	Expected (± (Stat.) ± (High p_T) ± (Low p_T))
4jSRb	1.0	15	23.6 ± 4.6 ± 6.1 ± 1.7
4jSR	1.0	82	68.2 ± 7.6 ± 15.8 ± 4.4
5jSRb	0.6	61	44.0 ± 7.5 ± 11.2 ± 7.2
5jSRb	0.8	10	7.0 ± 2.4 ± 1.9 ± 0.7
5jSR	0.8	31	18.0 ± 3.7 ± 4.6 ± 1.5

Table 2: Predicted and observed yields in various search regions in data for a number of different M_J^Σ cuts

Signal Region	M_J^Σ cut	Expected limit (fb)	Observed limit (fb)	p_0-value
4jSRb	> 1.0 TeV	$0.53^{+0.20}_{-0.12}$	0.37	0.5
4jSR		$1.12^{+0.50}_{-0.32}$	1.50	0.24
5jSRb	> 0.6 TeV	$0.86^{+0.40}_{-0.20}$	1.32	0.20
5jSRb	> 0.8 TeV	$0.24^{+0.10}_{-0.06}$	0.34	0.26
5jSR		$0.43^{+0.08}_{-0.06}$	0.84	0.062

Table 3: Expected and observed limits on the signal production cross section for the signal regions. The observed p_0-value is also shown.

$m_{\tilde{g}} \geq 1000$ GeV, the ratio of the detector level acceptance over truth level acceptance is between 0.95 and 1.10, for 4jSR with $M_J^\Sigma > 0.8$ TeV and 5jSR with $M_J^\Sigma > 0.6$ TeV. For signal regions with b-tagging requirements, 5jSRb with $M_J^\Sigma > 0.6$ TeV and 4jSRb with $M_J^\Sigma > 0.8$ TeV, this ratio drops to ≈ 0.75 - 0.98 for signal models with $m_{\tilde{\chi}_1^0} \geq 250$ GeV, and it is further reduced to ≈ 0.65 - 0.75, for signal models with small $m_{\tilde{\chi}_1^0}$ (e.g., $m_{\tilde{\chi}_1^0} <$ top mass), due to b-jets in signal events having higher p_T for which the b-tagging is less efficient. With 36.1 fb^{-1}at $\sqrt{s}$ = 13 TeV, the search has excluded a gluino with mass between 1000 GeV - 1875 GeV in the gluino cascade decay model, with the most stringent limit achieved at around $m_{\tilde{\chi}_1^0} \geq 1000$ GeV and the weakest limit achieved at around $m_{\tilde{\chi}_1^0} \geq 50$ GeV; for the gluino direct decay model, the search yields a limit on the production cross section between 0.011 fb^{-1} and 0.80 fb^{-1}, in the range of 900 GeV $< m_{\tilde{\chi}_1^0} <$ 1800 GeV.

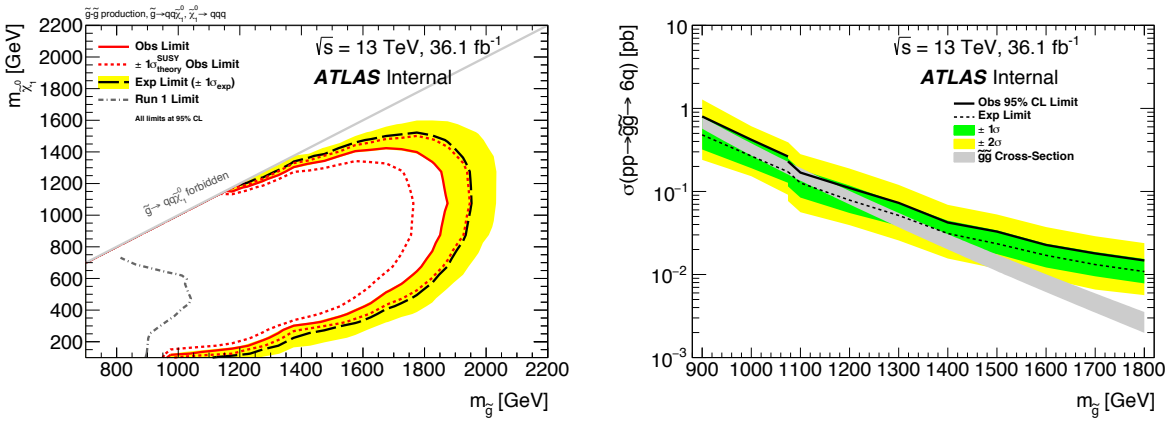

(a) gluino cascade decay model

(b) gluino direct decay model

Figure 7: (a) Expected and observed exclusion limits in the ($m_{\tilde{g}}$,$m_{\tilde{\chi}_1^0}$) plane for the gluino cascade decay model. Limits are obtained by using the signal region with the best expected sensitivity for every signal point (5jSRb with M_J^Σ > 0.6 TeV). The dashed black lines show the expected limits at 95% CL, with the light (yellow) bands indicating the ± 1 σ variations due to experimental uncertainties. Observed limits are indicated by medium dark (maroon) curves, where the solid contour represents the nominal limit, and the dotted lines are obtained by varying the signal cross section by the renormalization and factorization scale and PDF uncertainties. The observed limit from the Run-1 analysis [20] is also shown as a dotted-dashed line. (b) Expected and observed cross section limits for the gluino direct decay model gluino models. The discontinuities in the observed limit and ± 1 (2) σ bands are caused by the use of two different M_J^Σ cuts in the 5jSRb (> 0.6 TeV for $m_{\tilde{g}}$ < 1080 GeV, > 0.8 TeV for $m_{\tilde{g}}$ > 1080 GeV).

8 Conclusion

A search for R-Parity Violating SUSY signals in events with multiple jets is conducted. Distributions of events as a function of total jet mass are examined. No significant excess is seen in any signal regions. Limits are set on the production of gluinos in the gluino direct and cascade decay models in the UDD scenarios of RPV SUSY. In the gluino cascade decay model, gluinos with masses between 1000 GeV and 1875 GeV are excluded, depending on the neutralino mass; in the gluino direct decay model, signals with a cross section as small as 0.011 fb^{-1}- 0.8 fb^{-1} are excluded, depending on the gluino mass. Model-independent limits are also set on the signal production cross section in four overlapping signal regions. These significantly extend the limits from the 8 TeV LHC analyses.

Acknowledgements

We thank CERN for the very successful operation of the LHC, as well as the support staff from our institutions without whom ATLAS could not be operated efficiently.

We acknowledge the support of ANPCyT, Argentina; YerPhI, Armenia; ARC, Australia; BMWFW and FWF, Austria; ANAS, Azerbaijan; SSTC, Belarus; CNPq and FAPESP, Brazil; NSERC, NRC and CFI, Canada; CERN; CONICYT, Chile; CAS, MOST and NSFC, China; COLCIENCIAS, Colombia; MSMT CR, MPO CR and VSC CR, Czech Republic; DNRF and DNSRC, Denmark; IN2P3-CNRS, CEA-DSM/IRFU, France; SRNSF, Georgia; BMBF, HGF, and MPG, Germany; GSRT, Greece; RGC,

Hong Kong SAR, China; ISF, I-CORE and Benoziyo Center, Israel; INFN, Italy; MEXT and JSPS, Japan; CNRST, Morocco; NWO, Netherlands; RCN, Norway; MNiSW and NCN, Poland; FCT, Portugal; MNE/IFA, Romania; MES of Russia and NRC KI, Russian Federation; JINR; MESTD, Serbia; MSSR, Slovakia; ARRS and MIZŠ, Slovenia; DST/NRF, South Africa; MINECO, Spain; SRC and Wallenberg Foundation, Sweden; SERI, SNSF and Cantons of Bern and Geneva, Switzerland; MOST, Taiwan; TAEK, Turkey; STFC, United Kingdom; DOE and NSF, United States of America. In addition, individual groups and members have received support from BCKDF, the Canada Council, CANARIE, CRC, Compute Canada, FQRNT, and the Ontario Innovation Trust, Canada; EPLANET, ERC, ERDF, FP7, Horizon 2020 and Marie Skłodowska-Curie Actions, European Union; Investissements d'Avenir Labex and Idex, ANR, Région Auvergne and Fondation Partager le Savoir, France; DFG and AvH Foundation, Germany; Herakleitos, Thales and Aristeia programmes co-financed by EU-ESF and the Greek NSRF; BSF, GIF and Minerva, Israel; BRF, Norway; CERCA Programme Generalitat de Catalunya, Generalitat Valenciana, Spain; the Royal Society and Leverhulme Trust, United Kingdom.

The crucial computing support from all WLCG partners is acknowledged gratefully, in particular from CERN, the ATLAS Tier-1 facilities at TRIUMF (Canada), NDGF (Denmark, Norway, Sweden), CC-IN2P3 (France), KIT/GridKA (Germany), INFN-CNAF (Italy), NL-T1 (Netherlands), PIC (Spain), ASGC (Taiwan), RAL (UK) and BNL (USA), the Tier-2 facilities worldwide and large non-WLCG resource providers. Major contributors of computing resources are listed in Ref. [63].

References

[1] Y. A. Gol'fand and E. P. Likhtman,
Extension of the Algebra of Poincare Group Generators and Violation of p Invariance,
JETP Lett. **13** (1971) 323, [Pisma Zh.Eksp.Teor.Fiz.13:452-455,1971].

[2] D. V. Volkov and V. P. Akulov, *Is the Neutrino a Goldstone Particle?*, Phys. Lett. **B46** (1973) 109.

[3] J. Wess and B. Zumino, *Supergauge Transformations in Four-Dimensions*,
Nucl. Phys. **B70** (1974) 39.

[4] J. Wess and B. Zumino, *Supergauge Invariant Extension of Quantum Electrodynamics*,
Nucl. Phys. **B78** (1974) 1.

[5] S. Ferrara and B. Zumino, *Supergauge Invariant Yang-Mills Theories*,
Nucl. Phys. **B79** (1974) 413.

[6] A. Salam and J. A. Strathdee, *Supersymmetry and Nonabelian Gauges*,
Phys. Lett. **B51** (1974) 353.

[7] R. Barbieri and G. F. Giudice, *Upper Bounds on Supersymmetric Particle Masses*,
Nucl. Phys. **B306** (1988) 63.

[8] B. de Carlos and J. A. Casas, *One loop analysis of the electroweak breaking in supersymmetric models and the fine tuning problem*, Phys. Lett. **B309** (1993) 320,
arXiv: hep-ph/9303291 [hep-ph].

[9] G. R. Farrar and P. Fayet, *Phenomenology of the Production, Decay, and Detection of New Hadronic States Associated with Supersymmetry*, Phys. Lett. **B76** (1978) 575.

[10] L. J. Hall and M. Suzuki, *Explicit R-Parity Breaking in Supersymmetric Models*,
Nucl. Phys. **B231** (1984) 419.

[11] G. G. Ross and J. W. F. Valle, *Supersymmetric Models Without R-Parity*,
Phys. Lett. **B151** (1985) 375.

[12] V. D. Barger, G. F. Giudice and T. Han,
Some New Aspects of Supersymmetry R-Parity Violating Interactions,
Phys. Rev. **D40** (1989) 2987.

[13] H. K. Dreiner, *An Introduction to explicit R-parity violation*,
(1997), [Adv. Ser. Direct. High Energy Phys.21,565(2010)], arXiv: hep-ph/9707435 [hep-ph].

[14] R. Barbier et al., *R-parity violating supersymmetry*, Phys. Rept. **420** (2005) 1,
arXiv: hep-ph/0406039 [hep-ph].

[15] H. K. Dreiner, *An introduction to explicit R-parity violation*, Pramana **51** (1998) 123,
arXiv: hep-ph/9707435v2 [hep-ph].

[16] B. Allanach, A. Dedes and H. Dreiner, *R parity violating minimal supergravity model*,
Phys.Rev. **D69** (2004) 115002, arXiv: hep-ph/0309196 [hep-ph].

[17] E. Nikolidakis and C. Smith, *Minimal Flavor Violation, Seesaw, and R-parity*,
Phys. Rev. **D77** (2008) 015021, arXiv: 0710.3129 [hep-ph].

[18] C. Csaki, Y. Grossman and B. Heidenreich, *MFV SUSY: A Natural Theory for R-Parity Violation*,
Phys. Rev. **D85** (2012) 095009, arXiv: 1111.1239 [hep-ph].

[19] The ATLAS Collaboration, *Search for pair production of massive particles decaying into three quarks with the ATLAS detector in $\sqrt{s}$ = 7 TeV pp collisions at the LHC*, JHEP **12** (2012) 086, arXiv: 1210.4813 [hep-ex].

[20] The ATLAS Collaboration, *Search for massive supersymmetric particles decaying to many jets using the ATLAS detector in pp collisions at $\sqrt{s}$ = 8 TeV*, Phys. Rev. **D91** (2015) 112016, [Erratum: Phys. Rev.D93,no.3,039901(2016)], arXiv: 1502.05686 [hep-ex].

[21] The CMS Collaboration, *Searches for R-parity-violating supersymmetry in pp collisions at sqrt(s)=8 TeV in final states with 0-4 leptons*, (2016), arXiv: 1606.08076 [hep-ex].

[22] The ATLAS Collaboration, *The ATLAS Experiment at the CERN Large Hadron Collider*, JINST **3** (2008) S08003.

[23] M Capeans et al., *ATLAS Insertable B-Layer Technical Design Report*, (2010), ATLAS-TDR-19, URL: http://cds.cern.ch/record/1291633.

[24] The ATLAS Collaboration, *Performance of the ATLAS Trigger System in 2015*, Eur. Phys. J. **C77** (2017) 317, arXiv: 1611.09661 [hep-ex].

[25] J. Alwall et al., *The automated computation of tree-level and next-to-leading order differential cross sections, and their matching to parton shower simulations*, JHEP **07** (2014) 079, arXiv: 1405.0301 [hep-ph].

[26] T. Sjöstrand et al., *An Introduction to PYTHIA 8.2*, Comput. Phys. Commun. **191** (2015) 159, arXiv: 1410.3012 [hep-ph].

[27] The ATLAS Collaboration, *Summary of ATLAS Pythia 8 tunes*, (2012), ATL-PHYS-PUB-2012-003, URL: http://cds.cern.ch/record/1474107.

[28] R. D. Ball et al., *Parton distributions with LHC data*, Nucl. Phys. **B867** (2013) 244, arXiv: 1207.1303 [hep-ph].

[29] D. J. Lange, *The EvtGen particle decay simulation package*, Nucl. Instrum. Meth. **A462** (2001) 152.

[30] W. Beenakker et al., *Squark and gluino production at hadron colliders*, Nucl. Phys. **B492** (1997) 51, arXiv: hep-ph/9610490 [hep-ph].

[31] A. Kulesza and L. Motyka, *Threshold resummation for squark-antisquark and gluino-pair production at the LHC*, Phys. Rev. Lett. **102** (2009) 111802, arXiv: 0807.2405 [hep-ph].

[32] A. Kulesza and L. Motyka, *Soft gluon resummation for the production of gluino-gluino and squark-antisquark pairs at the LHC*, Phys. Rev. **D80** (2009) 095004, arXiv: 0905.4749 [hep-ph].

[33] W. Beenakker et al., *Soft-gluon resummation for squark and gluino hadroproduction*, JHEP **12** (2009) 041, arXiv: 0909.4418 [hep-ph].

[34] W. Beenakker et al., *Squark and Gluino Hadroproduction*, Int. J. Mod. Phys. **A26** (2011) 2637, arXiv: 1105.1110 [hep-ph].

[35] C. Borschensky et al., *Squark and gluino production cross sections in pp collisions at $\sqrt{s}$ = 13, 14, 33 and 100 TeV*, Eur. Phys. J. **C74** (2014) 3174, arXiv: 1407.5066 [hep-ph].

[36] J. Pumplin et al.,
New generation of parton distributions with uncertainties from global QCD analysis,
JHEP **07** (2002) 012, arXiv: hep-ph/0201195 [hep-ph].

[37] S. Schumann and F. Krauss,
A Parton shower algorithm based on Catani-Seymour dipole factorisation,
JHEP **0803** (2008) 038, arXiv: 0709.1027 [hep-ph].

[38] S. Hoeche et al., *QCD matrix elements and truncated showers*, JHEP **0905** (2009) 053,
arXiv: 0903.1219 [hep-ph].

[39] T. Gleisberg et al., *Event generation with SHERPA 1.1*, JHEP **02** (2009) 007,
arXiv: 0811.4622 [hep-ph].

[40] H.-L. Lai et al., *New parton distributions for collider physics*, Phys. Rev. **D82** (2010) 074024,
arXiv: 1007.2241 [hep-ph].

[41] S. Alioli et al., *A general framework for implementing NLO calculations in shower Monte Carlo programs: the POWHEG BOX*, JHEP **06** (2010) 043, arXiv: 1002.2581 [hep-ph].

[42] T. Sjostrand, S. Mrenna and P. Z. Skands, *PYTHIA 6.4 physics and manual*,
JHEP **0605** (2006) 026, arXiv: 0603175 [hep-ph].

[43] P. Z. Skands, *Tuning Monte Carlo Generators: The Perugia Tunes*, Phys. Rev. **D82** (2010) 074018,
arXiv: 1005.3457 [hep-ph].

[44] S. Agostinelli et al., *GEANT4: A Simulation toolkit*, Nucl. Instrum. Meth. **A506** (2003) 250.

[45] The ATLAS Collaboration, *The ATLAS Simulation Infrastructure*, Eur. Phys. J. **C70** (2010) 823,
arXiv: 1005.4568 [physics.ins-det].

[46] The ATLAS Collaboration,
The simulation principle and performance of the ATLAS fast calorimeter simulation FastCaloSim,
(2010), ATL-PHYS-PUB-2010-013, URL: http://cds.cern.ch/record/1300517.

[47] The ATLAS Collaboration,
Luminosity determination in pp collisions at $\sqrt{s} = 8$ TeV using the ATLAS detector at the LHC,
Eur. Phys. J. **C76** (2016) 653, arXiv: 1608.03953 [hep-ex].

[48] The ATLAS Collaboration,
Topological cell clustering in the ATLAS calorimeters and its performance in LHC Run 1,
Eur. Phys. J. **C77** (2017) 490, arXiv: 1603.02934 [hep-ex].

[49] T Barillari et al., *Local Hadronic Calibration*, (2008), ATL-LARG-PUB-2009-001-2.
ATL-COM-LARG-2008-006. ATL-LARG-PUB-2009-001,
URL: http://cds.cern.ch/record/1112035.

[50] S. Catani et al., *Longitudinally invariant K_t clustering algorithms for hadron hadron collisions*,
Nucl. Phys. **B406** (1993) 187.

[51] The ATLAS Collaboration, *Performance of jet substructure techniques for large-R jets in proton-proton collisions at $\sqrt{s} = 7$ TeV using the ATLAS detector*, JHEP **09** (2013) 076,
arXiv: 1306.4945 [hep-ex].

[52] D. Krohn, J. Thaler and L.-T. Wang, *Jet Trimming*, JHEP **02** (2010) 084,
arXiv: 0912.1342 [hep-ph].

[53] The ATLAS Collaboration, *Jet energy scale measurements and their systematic uncertainties in proton-proton collisions at $\sqrt{s}$ = 13 TeV with the ATLAS detector*, (2017), arXiv: 1703.09665 [hep-ex].

[54] ATLAS Collaboration, *Properties of jets and inputs to jet reconstruction and calibration with the ATLAS detector using proton–proton collisions at $\sqrt{s}$ = 13 TeV*, ATL-PHYS-PUB-2015-036, 2015, URL: https://cds.cern.ch/record/2044564.

[55] The ATLAS Collaboration, *Performance of b-Jet Identification in the ATLAS Experiment*, JINST **11** (2016) P04008, arXiv: 1512.01094 [hep-ex].

[56] The ATLAS Collaboration, *Optimisation of the ATLAS b-tagging performance for the 2016 LHC Run*, (2016), URL: http://cds.cern.ch/record/2160731.

[57] A. Hook et al., *High Multiplicity Searches at the LHC Using Jet Masses*, JHEP **3** (2012) 9, arXiv: 1202.0558.

[58] S. El Hedri et al., *Learning How to Count: A High Multiplicity Search for the LHC*, JHEP **08** (2013) 136, arXiv: 1302.1870.

[59] T. Cohen et al., *Jet Substructure Templates: Data-driven QCD Backgrounds for Fat Jet Searches*, JHEP **05** (2014) 005, arXiv: 1402.0516 [hep-ph].

[60] The ATLAS Collaboration, *Search for new phenomena in final states with large jet multiplicities and missing transverse momentum at $\sqrt{s}$=8 TeV proton-proton collisions using the ATLAS experiment*, JHEP **10** (2013) 130, [Erratum: JHEP01,109(2014)], arXiv: 1308.1841 [hep-ex].

[61] The ATLAS and CMS Collaborations, *Procedure for the LHC Higgs boson search combination in summer 2011*, (2011), CMS-NOTE-2011-005. ATL-PHYS-PUB-2011-11, URL: http://cds.cern.ch/record/1379837.

[62] A. L. Read, *Presentation of search results: the CL s technique*, Journal of Physics G: Nuclear and Particle Physics **28** (2002) 2693, URL: http://stacks.iop.org/0954-3899/28/i=10/a=313.

[63] ATLAS Collaboration, *ATLAS Computing Acknowledgements 2016–2017*, ATL-GEN-PUB-2016-002, URL: https://cds.cern.ch/record/2202407.